

## Nonlinear current-voltage characteristics of nanochannels

Gilad Yossifon, Peter Mushenheim, Yu-Chen Chang, and Hsueh-Chia Chang\*

*Department of Chemical and Biomolecular Engineering, Center for Microfluidics and Medical Diagnostics,  
University of Notre Dame, Notre Dame, Indiana 46556, USA*

(Received 14 October 2008; published 3 April 2009)

Like ion channels, nanochannels are known to exhibit curious non-Ohmic current-voltage ( $I$ - $V$ ) characteristics with an approximate piece-wise constant differential resistance. Using a nanoslot model and a nonequilibrium ion transport theory, we attribute the nonlinear resistance to overlapping double layers inside and an extended polarized layer of space charge outside the nanochannel. The overlimiting current beyond a critical voltage is shown to develop when the polarized layer is destabilized by a microvortex instability at one entrance. By extending earlier nanochannel and polarized layer models to include this instability, nonideal ion permselectivity and field-focusing effect, quantitative predictions—together with explicit differential resistance expressions—are offered for the nonlinear  $I$ - $V$  features of a nanochannel surrounded by microreservoirs from a simple pseudo-one-dimensional model.

DOI: 10.1103/PhysRevE.79.046305

PACS number(s): 47.61.Fg, 47.57.jd, 82.39.Wj, 47.20.Ma

### I. INTRODUCTION

A curious and important current-voltage ( $I$ - $V$ ) characteristic of conducting ion-selective (nanoporous) membranes, such as Nafion membranes in fuel cells, cell membranes with ion channels, and desalination membranes, is that—at sufficiently high voltages—the current density deviates from the usual linear Ohmic dependence on the voltage. More specifically [see Fig. 1(a) or Fig. 6(b)], at some current threshold, the differential resistance increases to a large, yet, finite value. Beyond a critical “gating” voltage, the differential resistance decreases again to a level that is comparable with that in the Ohmic region. The former part of the  $I$ - $V$  curve is referred to as the “limiting-resistance” region, while the latter is referred to as the “overlimiting current” region (e.g., [1]).

The threshold current at which the limiting-resistance region occurs is often approximated by the classical diffusion-limited current transport theory [2], according to which the current density saturates at a constant level known as the “limiting-current density” with an infinite differential resistance. An electroneutral diffusion layer with an ion concentration gradient appears near the membrane-electrolyte interface of depleted ionic concentration (where the counterion enters) to enhance the flux via diffusion. This diffusive-flux-enhanced current density saturates when both ion concentrations vanish at the surface [2]. There is yet no reported explanation of the large but finite differential resistance in the limiting-resistance region that is not captured in Levich’s limiting-current-density theory.

Latter theories by Rubinstein and Shtilman [3] suggested that, at high voltages, an extended polarized layer with space charge [EPL, or equivalently, space-charge layer (SCL)] much thicker than the electric Debye layer (EDL) can appear between the EDL and the electroneutral diffusion layer [DL, see Fig. 4(c)] to sustain an overlimiting-current density, much higher than the limiting-current density. The collection

of these three different layers is termed the concentration polarization layer (CPL). Starting with Rubinstein and Shtilman [3], latter studies have offered *one-dimensional* models of either an ideal [4] or nonideal [5] permselective nanoporous membrane. Such one-dimensional models treat the nanoporous membrane as a continuum and neglects field-focusing effects through the nanopores. The small cross-section area of the pore compared to the cross-section area of the same flux tube outside the pore enhances intrapore resistance to ion current. As a result, the omission of the field effect often mistakenly attributes the bulk region to the dominant resistance in the DL outside the membrane instead of a dominant intrapore resistance. More importantly, all earlier theories invoke an arbitrary CPL length, without specifying the physical mechanism that selects it. Consequently, neither the limiting-resistance region nor the overlimiting  $I$ - $V$  regions have been mechanistically explained or quantitatively captured.

Rubinstein *et al.* [6] were the first to suggest a possible mechanism for selecting the CPL dimension that involves an intrinsic instability of the SCL (see also [7] and references therein). The lateral osmotic-pressure gradient of this vortex instability produces a stationary vortex array (Fig. 2) that specifies the thickness of the CPL, which in turn, controls the overlimiting-current density. This mechanism, although consistent with some indirect experimental observations [1,8], was only recently verified experimentally [9].

In this paper, we integrate these present understandings of intramembrane and transmembrane ion transport mechanisms into a coherent theory that quantitatively captures all three  $I$ - $V$  regions of nanoporous membranes and favorably compared the theories to  $I$ - $V$  measurements across a nanoslot. A straight nanochannel or nanoslot is a simple model for an ion-selective nanoporous membrane, as the EDLs of both substrates overlap as in a nanopore. Like an ion-selective membrane, the overlapping double layers select the counterions to carry most of the current across the slot. In recent years, fabrication of nanochannels has become possible and the ion transport (e.g., [10]), ion enrichment and ion depletion (e.g., [11,12]), rectification of ionic current (e.g., [13]), and overlimiting-current [14] phenomena have

\*Corresponding author; hchang@nd.edu

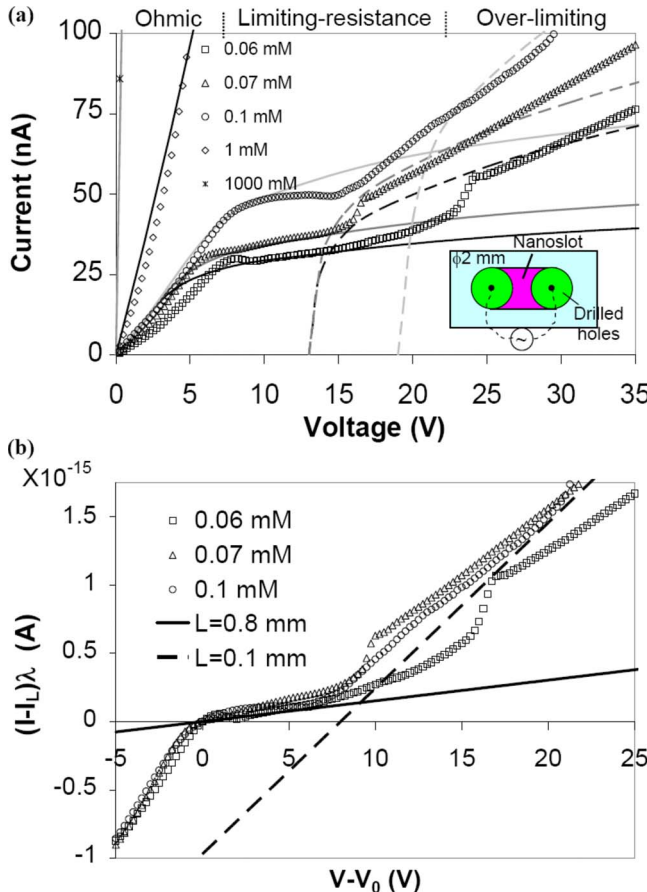


FIG. 1. (Color online) (a)  $I$ - $V$  characteristics of a nanoslot (inset) for varying ionic strengths [symbols—experiment; continuous lines—model ( $L=L_{\text{electrode}}=0.8$  mm); and dashed lines—model ( $L=L_{\text{instability}}=0.1$  mm)]; (b) collapse of large- $I$  data in (a) using Ben and Chang [4] theory (14a) (continuous line— $L=L_{\text{electrode}}$ ; dashed line— $L=L_{\text{instability}}$ ). The empirical limiting current  $\tilde{I}_L$  and threshold voltages  $V_0$  for each set of the experimental data are  $\tilde{I}_L(\text{exp})=29$  nA,  $V_0(\text{exp})=7.0$  V ( $c_0=0.06$  mM);  $\tilde{I}_L(\text{exp})=32$  nA,  $V_0(\text{exp})=6.0$  V ( $c_0=0.07$  mM); and  $\tilde{I}_L(\text{exp})=46$  nA,  $V_0(\text{exp})=8.0$  V ( $c_0=0.1$  mM). Note that these empirical values were used only in part (b) of the figure for collapsing the experimental data, while part (a) of the figure, which depicts the computational model results, does not need to account for any of these empirical values.

been examined with these pseudoion selective membranes. Here, we offer a comprehensive predictive theory for the nonlinear  $I$ - $V$  characteristics of nanoslots bounded by microreservoirs with explicit differential resistance expressions from a simple pseudo-one-dimensional model for the complex two-dimensional geometry.

## II. EXPERIMENTAL TECHNIQUES AND METHODS

A nanofluidic slot [inset of Fig. 1(a)] was fabricated following an anodic bonding procedure similar to that of Kutchoukov *et al.* [15]. Briefly, a nanoslot 2 mm wide and 4 mm long was patterned using standard photolithography techniques on a 250-nm-thick polysilicon layer deposited on a 1-mm-thick Pyrex glass (Corning 7740) substrate. A reactive

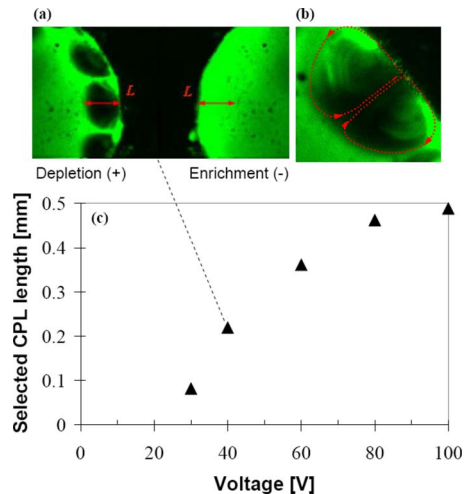


FIG. 2. (Color online) (a) Confocal image snapshots of the steady diffusion layer extent  $L$  in its either enrichment (cathodic polarity) or depletion (anodic polarity) phase at 40 V dc voltage level; (b) a closeup of one of the depletion regions showing its inner structure consisting of a vortex pair; and (c) the instability selected CPL length scale as a function of voltage for a buffer concentration of  $\sim 0.03$  mM (reprinted with permission [9]).

$\text{CF}_4/\text{O}_2$  plasma then etched into the polysilicon layer at a rate of 100 nm/min. The depth of the resulting channel was determined by the thickness of the polysilicon layer (i.e.,  $h=250$  nm) as was verified using an  $\alpha$ -stepper profilometer. The Pyrex slide was then sealed against another 1-mm-thick Pyrex slide with mechanically predrilled holes of  $\sim 2$  mm in diameter, after cleaning in  $\text{HNO}_3$  solution for about 10 min. To ensure good bonding, the wafers were preheated for 2 h at 400 °C and bonded at the same temperature at 1000 V for 1 h. The resulting average length of the nanoslot between the two holes was  $\sim 0.8$  mm. Reservoirs made of flexible silicon (FastwellTM from Grace bio-Laboratories) were used on top of the holes wherein platinum electrodes were introduced.

The nanoslot was filled by introducing distilled deionized (18 M  $\Omega\text{cm}$ ) water into the large fluidic reservoirs from which point capillary forces were sufficient to draw the water across the nanoslot. The electrical voltage source and  $I$ - $V$  converter (Agilent Technologies, 4155 B semiconductor parameter analyzer) were connected to the fluidic channel with negligible resistive loss via platinum wires inserted into the reservoirs. The channels were cleaned of ionic contaminants using the electrophoretic pumping. The ionic current was observed to decay while 10 V were applied across the channels to drive out ionic impurities. The reservoirs were periodically flushed with fresh solution until the current equilibrated to a minimum, which typically took  $\sim 20$  min. This procedure was also followed to replace different dilutions of 1 M potassium chloride (KCl) to change the ionic strength and control the degree of EDL overlap.

To obtain the measured  $I$ - $V$  curves in Fig. 1, the applied voltage was stepped in 0.25 V increments every 3 s, during which time current transients were observed to decay completely. In the low-concentration limit, the three distinct  $I$ - $V$  regimes are indeed observed: a linear Ohmic region, followed by a limiting-resistance region with a small slope

(large limiting differential resistance), and finally an overlimiting region [Fig. 1(a)]. These data are in qualitative agreement with previous experimentally obtained  $I$ - $V$  curves for true nanoporous membranes ([1,8]) and also for nanochannels [14].

At high enough concentrations ( $>10^{-3}$  M), only the Ohmic region is observed as the thinner Debye length stipulates that EDLs overlap within the slot and the nanochannel's permselectivity, space charge, and superior conductivity are lost—it is no longer a model for an ion-selective nanoporous membrane. Space-charge accumulation at and across the slot-bulk interface is responsible for the formation of the polarized layer. Such space-charge accumulation is only possible with a conductivity jump at the interface and hence, at high ionic strengths, the nanochannel contains electroneutral bulk electrolytes and behaves like the bulk Ohmic resistor but with a larger resistance.

In contrast, the nanoslot ion distribution becomes important at low ionic strengths and produces all three regimes of the  $I$ - $V$  curve. Note, however, the conductance at this low-voltage Ohmic region does not scale linearly with the low bulk ionic strength [Fig. 5], suggesting that the intraslot resistance is important. Ohmic resistance is hence not just due to external resistance, as is assumed in earlier theories involving an infinitely conducting membrane. The conductivity within the slot is finite and must be considered to quantitatively capture the true  $I$ - $V$  characteristics. However, in the limiting resistance and overlimiting-current region, the  $I$ - $V$  curves are again sensitive to the low bulk ionic strength, suggesting that the bottle-neck resistance now shifts away from the nanoslot to the bulk.

In order to visualize the polarized regions, we used positive-charged (cation) Rhodamine 6G fluorescent dye molecules (counterions of the nanoslot) of  $10 \mu\text{M}$  concentration (see [9] for more detailed description). When a  $40 \text{ V}$  dc field is applied across the nanoslot, an enrichment region at the cathodic entrance of the nanoslot is observed with high dye concentration while a depletion region is observed at the anodic side where the dye enters the nanoslot, as seen in Fig. 2(a). A peculiar pattern formation is observed on the depletion side, while no such pattern exists on the enrichment layer. This is in agreement with the vortex instability theory of Rubinstein *et al.* [6], which stipulated that an unstable EPL only exists in the depletion region (a combination of DL and EPL, hence, approximates the entire CPL thickness). Part (b) of Fig. 2 is a blowup of one such depletion region revealing its inner structure, which consists of a vortex pair with dye streaks that resemble the streamlines from the simulation of Rubinstein and Zaltzman [16]. The fact that this pattern formation corresponds to the vortex array of Rubinstein *et al.*'s [6] theory was proven recently in Yossifon and Chang [9] (see also the supplementary video linked to [9]). It is found in [9] that the vortex instability arrests the self-similar diffusive growth of the depletion layer and this in turn selects the overlimiting current. We find the thickness of the depletion layer at one entrance to be comparable to that in the enrichment region in the other. However, due to the low ionic strength in the depletion layer, it is quite obvious that it is the depletion layer that controls the current and the thickness of both layers. The vortices only appear at the

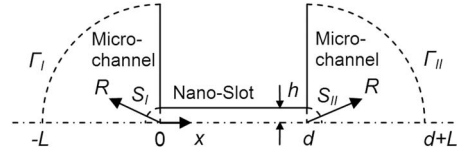


FIG. 3. Schematic description of the two-sided micronanochannel junction geometry of a nanoslot viewed in profile.

depletion layer beyond a critical voltage of about  $20 \text{ V}$  [9]. Below this voltage, the CPL extends to the electrode and beyond it the vortices select a *smaller* CPL dimension that increases monotonically with voltage, as shown in Fig. 2(c). When the voltage exceeds that for the Ohmic region, where intraslot resistance dominates, these observations suggest that the CPL on the depletion layer side controls the current, thus explaining the sensitivity to bulk ionic strength in these higher-voltage regions.

### III. THEORETICAL MODEL

A nonideal permselective membrane necessitates a model for membranes of finite conductance and a theory that couples all three domains of the problem (i.e., both the CPLs at the anodic and cathodic sides of the membrane and the nanopore). We employ Manzanares *et al.*'s [5] simplified model for a nonideally permselective one-dimensional nanoporous membrane, in which the surface charge is included in the averaging of the ion transport and Poisson equations across both solid and liquid phases to produce an effective homogeneous model. The membrane is assumed to contain fixed charged groups at a uniform volumetric concentration density  $\Sigma$ . This model is extended to the nanoslot geometry here with matching conditions at the entrance to capture the field-focusing effect that arises from the two dimensionality of the slot. The same field-focusing effect also occurs for true membranes but has yet to be scrutinized.

Figure 3 depicts schematically the two-sided micro-nanochannel junction problem geometry of a nanoslot *viewed in profile*. We use a polar coordinate system ( $R$ ) in the microregions and a Cartesian coordinate system ( $x$ ) inside the intrananoslot. The two-dimensional problem can be further simplified into an effective one-dimensional problem by assuming radial symmetry in the microchannel regions and treating only axial changes within the nanochannel region. This assumption is valid because the nanoslot height  $h$  is much smaller than the depth and lateral dimensions (or equivalently, the radius of curvature) of the microreservoir [inset of Fig. 1(a)]. Both the enrichment region and the depletion region in the two entrances are assigned the CPL length  $L$ . By appropriate coordinate transformation (i.e.,  $x = -R$  at  $-L < x < -h$  and  $x = d + R$  at  $d + h < x < d + L$ , where  $d$  is the nanochannel length), we can describe all three domains in terms of one axial coordinate  $x$ .

We chose the following normalization for the axial coordinate  $\tilde{x} = Lx$ , time  $\tilde{t} = (L^2/D)t$ , ionic concentration  $\tilde{c} = c_0 c$ , electric potential  $\tilde{\phi} = (RT/zF)\phi$ , ionic flux density  $\tilde{j} = (Dc_0/L)j$ , and electric current density  $\tilde{i} = (FzDc_0/L)i$ . Here,

the tilde stands for dimensional parameters,  $c_0$  is the buffer solution concentration,  $F$  denotes the Faraday number,  $z$  is the ion valency,  $R$  is the universal gas constant,  $T$  is the absolute temperature, and  $D$  is the ionic diffusion coefficient. We also define the nondimensional parameter  $\delta = \lambda/L$  as the ratio between the EDL length scale  $\lambda = \sqrt{\varepsilon_0 \varepsilon_f R T / 2 z^2 F^2 c}$  and the CPL length  $L$ . Herein,  $\varepsilon_0$  is the electric permittivity of vacuum and  $\varepsilon_f$  denotes the dielectric constant of the electrolyte solution.

Since there is no external stirring in our microdevice and our micronanochannel junction [inset of Fig. 1(a)] is nearly planar and perpendicular to the applied electric field, we do not expect an electro-osmotic (EO) vortex of the second kind [17] to develop. Moreover, due to the flow continuity into the nanoslot, the net flow rate of any through flow in the microreservoirs—where the depletion layer resides—must be equal to that in the nanoslot of a minute cross-section area. Consequently, the average velocity in the depletion layer is extremely small, and the EO convective contribution to both the instability and ionic transport is negligible. This is consistent with previous works on nanoporous membranes in

which a one-dimensional *quiescent* electrodiffusioconduction model was used, while totally neglecting convection effects [3–5]. While this is certainly true for the Ohmic and limiting resistance regions wherein no vortex instability exists, it is also true for the overlimiting region (beyond the critical voltage at which the vortex instability kicks in). The vortex convective flow does not contribute to the net ionic current into the nanoslot, as its net convection flux from the microreservoir into the nanoslot is zero. This is again consistent with previous works on vortex instability in which a zero normal velocity component was taken as a boundary condition, at the membrane-electrolyte interface, for the hydrodynamic problem [6,7]. Hence, also in the overlimiting region, it is commonly assumed that only an electrodiffusiocontribution to the ionic conduction exists [3–5].

A symmetric electrolyte ( $z^+ = -z^- = z$ ) of equal diffusivities ( $D^+ = D^- = D$ ) is assumed to simplify the analysis. Thus,  $\phi$  and  $c^\pm$  satisfy the following (Nernst-Planck) equations for the ionic species in the three domains, with radial symmetry invoked in the microreservoirs:

$$\frac{\partial c^\pm}{\partial t} = \begin{cases} \left( \frac{\partial}{\partial x} + \frac{1}{x} \right) \left( \frac{\partial c^\pm}{\partial x} \pm c^\pm \frac{\partial \phi}{\partial x} \right) & \text{at } -1 < x < -\frac{h}{L} \\ \frac{\partial}{\partial x} \left( \frac{\partial c^\pm}{\partial x} \pm c^\pm \frac{\partial \phi}{\partial x} \right) & \text{at } -\frac{h}{L} < x < \frac{d+h}{L} \\ \left( \frac{\partial}{\partial x} + \frac{1}{x-d/L} \right) \left( \frac{\partial c^\pm}{\partial x} \pm c^\pm \frac{\partial \phi}{\partial x} \right) & \text{at } \frac{d+h}{L} < x < \frac{d+L}{L}, \end{cases} \quad (1)$$

and the corresponding Poisson's equation for the three domains are

$$\begin{cases} \frac{1}{x} \frac{\partial}{\partial x} \left( x \frac{\partial \phi}{\partial x} \right) = -\frac{c^+ - c^-}{2\delta^2} & \text{at } -1 < x < -\frac{h}{L} \\ \frac{\partial^2 \phi}{\partial x^2} = -\frac{c^+ - c^- - \Sigma}{2\delta^2} & \text{at } -\frac{h}{L} < x < \frac{d+h}{L} \\ \frac{1}{x-d/L} \frac{\partial}{\partial x} \left[ \left( x - \frac{d}{L} \right) \frac{\partial \phi}{\partial x} \right] = -\frac{c^+ - c^-}{2\delta^2} & \text{at } \frac{d+h}{L} < x < \frac{d+L}{L}, \end{cases} \quad (2)$$

where  $\Sigma$  is the effective fixed volumetric charge (normalized by  $c_0$ ) from the surface charge that allows a one-dimensional formulation within the nanoslot [5]. The radially symmetric model for the microreservoirs allows us to also model these strictly complex two-dimensional regions with a convenient pseudo-one-dimensional model.

The CPL thickness  $L$  is the electrode separation from the entrance  $L_{\text{electrode}}$  for voltages below the onset of the vortex instability in Fig. 2(c). Beyond that voltage, it is assigned the measured vortex-selected value  $L_{\text{instability}}$  in Fig. 2(c), which is much smaller than  $L_{\text{electrode}}$  but is still larger than the channel slot depth  $h$ .

At the interface between the diffusion layer and the Ohmic bulk solution (i.e.,  $\tilde{R}=L$ ),  $\phi$  and  $c^\pm$  satisfy the electrostatic conditions

$$\frac{\partial \phi}{\partial x} = -I/\pi \quad \text{at } x = -1(\Gamma_I), \quad (3a)$$

$$\phi = 0 \quad \text{at } x = 1 + d/L(\Gamma_{II}), \quad (3b)$$

and the equality of the ionic concentrations to that of the buffer solution concentration  $c_0$

$$c^\pm = 1 \quad \text{at } x = -1(\Gamma_I), \quad x = 1 + d/L(\Gamma_{II}). \quad (4)$$

In Eq. (3)  $I$  is the imposed electric current (per unit width

normal to the plane of Fig. 3 normalized by  $FzDc_0$ ) through  $\Gamma_I$ . Furthermore, for future reference, the electric potential drop across the system (i.e., between  $\Gamma_I$  and  $\Gamma_{II}$ ) is designated as  $V$ .

At the interface between the nanochannel and microchannel (i.e.,  $\tilde{R}=h$ ), we impose the matching conditions of electric field  $E$  and ionic flux  $j^\pm$  continuity to capture the field and flux focusing effects,

$$(E)_R = (E)_x 2/\pi$$

$$(j^\pm)_R = (j^\pm)_x 2/\pi. \quad (5)$$

at  $x=-h/L(S_I)$ ,  $x=d/L+h/L(S_{II})$ .

#### IV. LIMITING-CURRENT DENSITIES, FIELD-FOCUSING, AND POLARIZED LAYERS

An analog of Levich's limiting-current density can be theoretically estimated for this geometry by including field-focusing effects, as a first-order approximation of the limiting-resistance region in Fig. 1. Taking into account also a finite intraslot conductance, instead of the common assumption of an infinite conductance [2–4], allows us to consider the nonideal ion permselective case as well. The limiting current occurs when the concentration gradient becomes significant at higher voltages and the ionic concentration at the anodic membrane-electrolyte interface ( $x=-h/L$ ) approaches zero. As this occurs, the bottle neck for current flux shifts from the nanoslot to the bulk and the bulk resistance becomes relevant. If one neglects the development of another current-controlling-extended polarized layer at the interface in this limit—as was assumed by Levich's theory—and retains the electroneutrality condition ( $c^+ = c^- = c$ ), the resulting ionic fluxes at the anodic side of the nanochannel are

$$j^\pm = -\left(\frac{\partial c}{\partial x} \pm c \frac{\partial \phi}{\partial x}\right), \quad (6)$$

from which one obtains for the radial geometry outside the nanoslot

$$\frac{\partial c}{\partial x} = -\frac{j^+ + j^-}{2} = \frac{1}{\pi} \frac{J^+ + J^-}{x}, \quad (7)$$

where  $J^\pm$  is the steady ionic flux through the sector of circle  $R=-x$  and the  $x$  term in the denominator on the right captures the field- and flux-focusing effects of the radial geometry. Unlike  $j^\pm$ , which represents the flux density (flux per unit area),  $J^\pm$  represents the flux per unit width after integrating the flux density over the height of the nanoslot.

Combining Eq. (7) with Eq. (4) yields the following nonlinear concentration profile in the DL [see Fig. 4(e)]:

$$c = 1 + \frac{J^+ + J^-}{\pi} \ln(-x) \quad \text{at} \quad -1 < x < -h/L. \quad (8)$$

Imposing the limiting-current condition  $c=0$  at  $x=-h/L (S_I)$  on Eq. (8) yields  $J^+ + J^- = -\pi/\ln(h/L)$ . The radial geometry that focuses the field into the slot is responsible for a large logarithm reduction in the current corresponding to the ratio

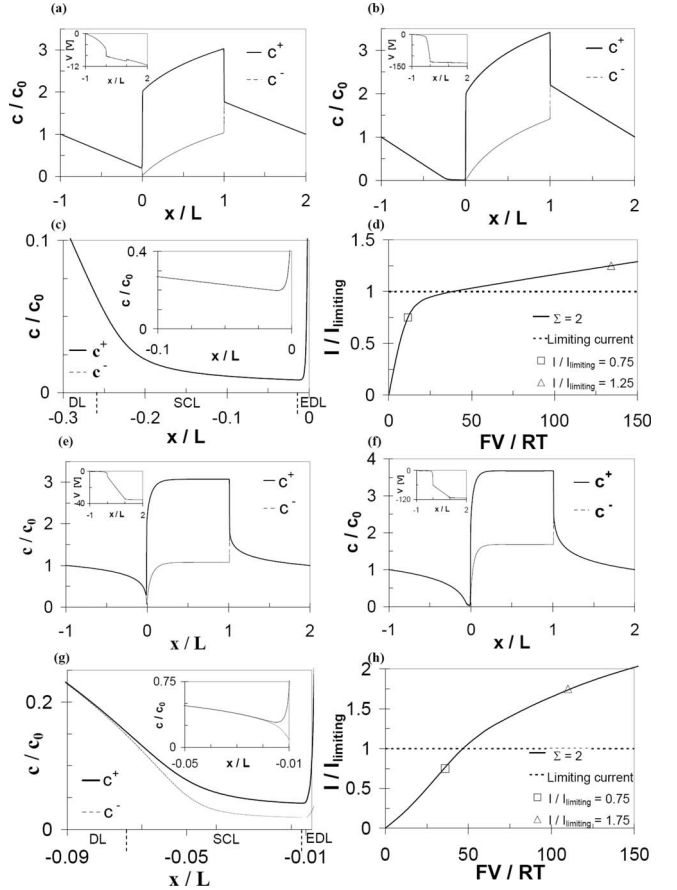


FIG. 4. Numerical computation results for the concentration polarization profiles across a *one-dimensional* membrane ( $0 \leq x \leq 1$ ) for currents below (a) and beyond (b) the limiting current  $I_L$ . The insets of parts (a) and (b) of the figure describe the potential drop across the system. Part (c) of the figure depicts the ion concentration profiles on the anodic side of the membrane for the overlimiting conditions of (b), exhibiting an SCL, in contrast to the profile of (a) in the inset. Also depicted are the electroneutral DL and the EDL. The  $I$ - $V$  curve for the membrane, exhibiting an inflection point at  $I_L$ , is shown in (d) with the conditions for (a) and (b) indicated. The normalized values of  $\Sigma=2$ ,  $d=1$ , and  $\delta=10^{-3}$  have been used. Parts (e)–(h) of the figure are the same as (a)–(d) but for the nanoslot geometry of Fig. 3 with an arbitrary ratio of  $h/L=10^{-2}$ .

of the diffusion layer thickness to the nanoslot depth, which is typically on the order of  $10^4$ . This electric current per unit width  $I=J^+-J^-$  results in the following expression for the limiting current per unit width (normalized by  $FzDc_0$ ):

$$I_L = -\frac{\pi}{\ln(h/L)} \left( \frac{\eta+1}{\eta-1} \right), \quad (9)$$

wherein  $\eta = -J^+/J^-$  is the ratio between the counterion and coion fluxes (assuming that the nanoslot surface is negatively charged) and is related to the permselectivity of the membrane system. For an ideal permselective membrane (i.e.,  $\eta \rightarrow \infty$ ), we obtain  $I_L|_{\eta \rightarrow \infty} = -\frac{\pi}{\ln(h/L)}$ . Following Manzanares *et al.* [5] [Eq. (16)]  $\eta$  is related to  $\Sigma$  through the ratio of the counterion to coion concentration *within* the membrane  $\eta$

$=c^+(\Sigma)/c^-(\Sigma)$  at  $-h/L < x < d/L + h/L$ , wherein explicit expressions for  $c^\pm(\Sigma)$  are given in Eq. (12). It is obvious from Eq. (2) that within the membrane nanopore this ratio increases with  $\Sigma$ . Also, from Eq. (9) it is clear that the normalized limiting current  $I_L$  monotonically increases as the perm-selectivity degree  $\eta$  decreases.

In contrast, using the above approach but for a *one-dimensional* membrane (as in [5]) yields a linear DL concentration profile [see Fig. 4(a)],

$$c = 1 - \frac{j^+ + j^-}{2}(x + 1) \quad \text{at} \quad -1 < x < -h/L, \quad (10)$$

instead of the logarithmic profile (8) and produces a limiting-current density (normalized by  $FzDc_0/L$ ) of the form

$$i_L = 2 \left( \frac{\eta + 1}{\eta - 1} \right), \quad (11)$$

with the familiar asymptotic limit of  $i_L = 2$  for an ideal perm-selective membrane ( $\eta \rightarrow \infty$ ) (e.g., [4]). The extra logarithm geometric term in Eq. (9) is due to field-focusing effects, which lowers the limiting current. We also note that our pseudo-one-dimensional model actually captures the entire two-dimensional sector of the nanoslot microreservoir (Fig. 3). Hence, the scaling of the current per unit width in Eq. (9) and the current density in Eq. (11) are off by the scaling length  $L$ .

However, the limiting-current density in Eq. (9) only estimates the current density at the limiting-resistance region and not its differential resistance. The dominance of intraslot resistance occurs because of field focusing into the nanoslot—all the current must go through the nanoslot and the converging field produces a high current density from the bulk in Eq. (9) that blows up as logarithmically with respect to the large ratio of the CPL thickness to the nanochannel height. To sustain this high Ohmic current from the bulk, a polarized layer develops as the bulk concentration at the interface approaches zero to introduce a larger field for flux into the slot [3]. With the appearance of the polarized layer, the electroneutral assumption of the limiting-current theory breaks down and a finite differential resistance develops at the anodic CPL.

The development of the polarized region can be captured numerically using the above effectively one-dimensional formulation. The distinct dc ion distributions and *I-V* characteristics in the Ohmic and overlimiting-current regimes are demonstrated for a one-dimensional membrane in parts (a)–(d) of Fig. 4 and for a nanoslot in parts (e)–(h) of Fig. 4. All computations are done with one specific CPL thickness  $L$ . Note that the depletion side on the left, where the bulk concentration  $c$  approaches zero, controls the *I-V* characteristics and contains significant space charge in its EPL. The enrichment side on the right with an ionic concentration higher than the bulk is always electroneutral (outside the thin equilibrium EDL) without a polarized layer. The polarized layer is obviously more pronounced with the field-focusing effect. It is this polarized layer amplified by the field-focusing effect on the depletion side that invalidates the classical limiting-current theory involving only electroneutral bulk transport.

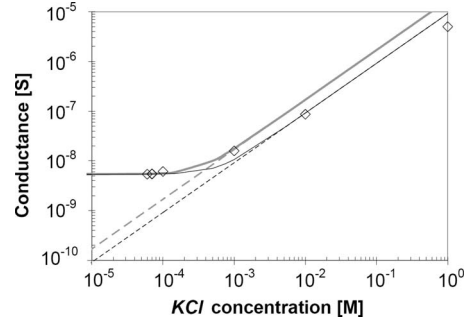


FIG. 5. Conductance of aqueous-filled polysilicon/Pyrex glass nanoslot as a function of  $c_0$ . Symbols—experiment; continuous thick gray line—model (13) with  $\mu = 14 \times 10^{-8} \text{ m}^2/\text{Vs}$ ; dashed thick gray line—bulk conductivity [model (13) with  $\tilde{\Sigma} = 0$ ] with  $\mu = 14 \times 10^{-8} \text{ m}^2/\text{Vs}$ ; continuous thin black line—model (13) with  $\mu = 7.6 \times 10^{-8} \text{ m}^2/\text{Vs}$ ; and dashed thin black line—bulk conductivity [model (13) with  $\tilde{\Sigma} = 0$ ] with  $\mu = 7.6 \times 10^{-8} \text{ m}^2/\text{Vs}$ .

## V. DIFFERENTIAL RESISTANCE ESTIMATES FOR THE THREE *I-V* REGIMES

From the inset of Fig. 4(f), it is clear that the resistance is negligible in the cathodic enrichment side and the intraslot and CPL layer resistance on the anodic depletion side control the ion current flux. The anodic CPL resistance is further broken down into two parts: SCL and DL. As is evident in Figs. 4(a) and 4(e), the SCL layer does not exist in the Ohmic region of the *I-V* curve. The  $\ln(-x)$  DL concentration profile of Eq. (8) due to field focusing is obviously smaller than the linear profile (10) of a one-dimensional model, as is reflected by the smaller potential drop in Fig. 4(e) relative to Fig. 4(a). Consequently, with field focusing, the nanoslot resistance dominates over DL resistance as seen in the inset of Fig. 4(e) for the radial model, while the opposite is true for the one-dimensional membrane model, as seen in the inset of Fig. 4(a). This dominance of nanoslot resistance in the Ohmic region is dependent on the relative length of the microreservoir and the nanoslot. However, when the two are comparable, the much smaller nanoslot cross-section area and the radial potential drop outside it often combine to produce an Ohmic region that is controlled by the nanoslot resistance. As the conductance of the nanoslot in the low-concentration limit is specified by the total surface charge, the resistance in this region has a very different dependence on the ionic strength for a slot whose height is much larger than the Debye layer.

We analyze the Ohmic region of the data in Fig. 1 to obtain the surface charge density in the form of  $\Sigma$  in the model of Eq. (2). The dc conductance was determined by fitting the slope of the ionic current as a function of the applied voltage [Fig. 5]. At high  $c_0$ , where  $\kappa h \gg 1$  ( $\kappa = \lambda^{-1}$ ), the conductance  $\tilde{I}/\tilde{V} = 2zF\mu c_0 wh/d$  is linear with  $c_0$ , as is consistent with bulk electrolyte conductance. At low  $c_0$ , where  $\kappa h \ll 1$  and the surface charge density is  $2|\sigma| \gg zFc_0h$ , the conductance is independent of  $h$  and  $c_0$ , behaving as  $\tilde{I}/\tilde{V} \approx 2|\sigma|\mu w/d$  (wherein  $\mu = zF\nu = zFD/(RT)$  is the ion mobility,  $w$  is the nanoslot width,  $d$  is the nanochannel length, and the factor 2 stands for both the top and bottom walls of

the nanoslot while the side walls are neglected). The constant conductance reflects the fact that the nanoslot ions are mostly counterions and, due to electroneutrality, their number is equal to the total surface charge independent of bulk ionic strength or slot height. As is consistent with our model, the conductance enhancement due to electroosmosis has been neglected. For the nanoslot parameters (inset of Fig. 1)  $h = 250$  nm,  $d = 0.8$  mm,  $w = 2$  mm, and KCl solution parameters  $z = 1$ ,  $\mu = 7.6 \times 10^{-8}$  m<sup>2</sup>/Vs [18], a fitted value of  $|\sigma| = 7.7$  mC/m<sup>2</sup> for the surface charge density (inside the measured surface charge-density range of 2–100 mC/m<sup>2</sup> reported in [19] for similar substrates) was obtained from the low  $c_0$  data of Fig. 5. The counterion concentration with overlapping layer  $2|\sigma|/zFh$  is then about 1 mM, which is much larger than the bulk concentration of  $\sim 10$  μM.

Following Manzanares *et al.* [5], we substitute the surface charge density  $\sigma$  by a fixed volume charge density  $zF\tilde{\Sigma} = -2\sigma/h$  of about  $\sim 61$  KC/m<sup>3</sup>. Based on the well-known Donnan equilibrium relations [5], the ionic concentrations *within* the nanoslot can be expressed as

$$\tilde{c}^\pm = \pm \tilde{\Sigma}/2 + \sqrt{(\tilde{\Sigma}/2)^2 + c_0^2} \quad \text{at } 0 \leq \tilde{x} \leq d. \quad (12)$$

This produces a universal ionic conductance [20] for the intraslot dominating Ohmic region,

$$\tilde{I}/\tilde{V} = \left( F^2 \sum z_i^2 \nu_i \tilde{c}_i \right) wh/d = 2F\mu \sqrt{(\tilde{\Sigma}/2)^2 + c_0^2} wh/d, \quad (13)$$

which reduces to  $\tilde{I}/\tilde{V} = 2zF\mu c_0 wh/d$  in the limit of high concentrations  $c_0 \gg \tilde{\Sigma}$  and to  $\tilde{I}/\tilde{V} \approx zF\mu \tilde{c}^+ wh/d = -2\sigma\mu w/d$  in the limit of low concentrations  $c_0 \ll \tilde{\Sigma}$ . As expected, the latter is dominated by the counterions  $\tilde{c}^+$ , whereas the coions  $\tilde{c}^-$  are excluded from the nanochannel. As seen in Fig. 5, a good agreement is obtained between the model (13) (thin black continuous line) and the experimentally measured Ohmic data. Also depicted in Fig. 5 is the expected bulk conductance (thin black dashed line) as obtained from model (13) while neglecting the effect of the nanochannel surface charge, i.e.,  $\tilde{\Sigma} = 0$ . A clear deviation from this bulk conductance is clearly seen to occur at concentrations of about 1 mM, indicating that ion permselective effects become dominant at ionic strengths below this value. That Eq. (13) quantitatively captures the experimental results for the nanochannel conductance dependence on the bulk concentration (Fig. 5) justifies the neglect of electro-osmotic convection contribution to ion transport within the nanochannel regime in our model [Eqs. (1)–(5)]. Furthermore, due to a factor of more than  $10^3$  in the microreservoir and nanoslot heights, flow continuity implies that the velocity in the bulk is  $10^3$  times smaller than that in the nanochannel. Since convection contribution to the current can be neglected in the nanochannel, it is even more true outside the nanoslot, as is assumed in our model [Eqs. (1)–(5)].

The polarized layer SCL develops in the limiting-resistance and overlimiting regions such that it offers the dominant resistance, as the ionic species are almost completely depleted within it (insets of Figs. 4(b) and 4(f)]. In

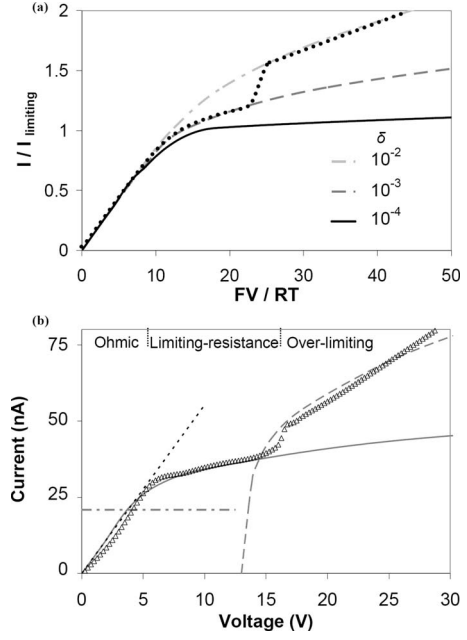


FIG. 6. (a) numerically calculated  $I$ - $V$  curves for varying  $\delta = \lambda/L$  in the case of an ideally permselective membrane. The dotted curve relates to the hypothesized change in the CPL length scale when the instability kicks in; (b) application of the suggested mechanism in (a) for the case of 0.07 mM concentration [symbol—experimental data; continuous line—model ( $L = 0.8$  mm); dashed line—model ( $L = 0.1$  mm); dotted line—asymptotic Ohmic region (13); and dashed-dotted line—limiting current (9)]. The normalized values of  $\Sigma = 10$ ,  $d = 1$ , and  $h/L = 10^{-2}$  have been used.

Fig. 4, a specific CPL length  $L$  is used and only one of the two regions is captured in the computed  $I$ - $V$  curves. However, as seen from Fig. 2(c),  $L$  actually changes from  $L_{\text{electrode}}$  in the limiting-resistance region to the much smaller value  $L_{\text{instability}}$  determined by the vortex instability [6] in the over-limiting region. Using  $L_{\text{electrode}} \sim 0.8$  mm (which is comparable to the distance between the nanoslot and the electrode) and an adjusted ion mobility of  $\mu = 14 \times 10^{-8}$  m<sup>2</sup>/Vs (which is a factor of 1.85 larger than the literature value [18]), our model [Eqs. (1)–(5)] yield the continuous curves in Fig. 1 for different buffer concentrations, which quantitatively capture both the Ohmic and limiting-resistance regions. As is consistent with the data, our model also faithfully captures the high-concentration region when the double layers do not overlap and the Ohmic region prevails over all voltages, owing to the loss of the nanoslot ionic permselectivity. The adjusted ion mobility value was chosen by fitting model [Eqs. (1)–(5)] for the limiting resistance current to the experimental data of a single bulk concentration [0.07 mM as seen in Fig. 6(b)], and this value is then used for the other concentrations. For coherency, instead of using two different ionic mobility values, i.e., for the Ohmic and non-Ohmic regions, a single value of  $\mu = 14 \times 10^{-8}$  m<sup>2</sup>/Vs was chosen to produce the *overall* best fit. Although this results in some deviation from the desired Ohmic conductance results (thick gray lines of Fig. 5), it is restricted to the high-concentration limit; whereas in the low-concentration limit the differences are negligible as we used a new fitted value of  $|\sigma|$

$=14.2$  mC/m<sup>2</sup> for the surface charge density. As the adjusted ionic mobility is associated with the transition to the limiting resistance region, hence controlled by the polarized layer outside the nanochannel (wherein the convection is smaller by a factor of at least  $10^3$  from that in the nanochannel), it is obvious that it cannot be attributed to electroconvection current enhancement but to other factors (e.g., geometrical, material properties, etc.). In any case, this factor of 1.85 between the fitted ionic mobility and that of the literature is very reasonable, considering the fact that a simple pseudo-one-dimensional model captures the *I-V* features of the complex three-dimensional model system described in the inset of Fig. 1(a).

However, when  $L$  is switched to a smaller  $L_{\text{instability}}$  (i.e., larger  $\delta=\lambda/L$ , while  $\lambda$  is kept constant) in Fig. 6(a), corresponding to supercritical voltages of Fig. 2(c), a different overlimiting region with a higher conductance develops. Hence, the two overlimiting regions of our model, corresponding to two different  $L$ , actually capture the limiting resistance and the overlimiting regimes of the *I-V* data. Figure 6(a) numerically demonstrates that the differential resistance (i.e., inverse of the slope) of the overlimiting region decreases with decreasing CPL thickness  $L$ , as represented by the parameter  $\delta=\lambda/L$ , while all other parameters are kept constant. As expected, a smaller CPL length increases the ion flux.

The solution of Eqs. (1)–(5) with a typical instability selected CPL length of  $L_{\text{instability}}=0.1$  mm [Fig. 2(c)] is also depicted in Fig. 1 as dashed lines for the different buffer concentrations. Although, as expected, the CPL length does not have any influence on the Ohmic region, it results in an overlimiting current of a higher slope, which is quantitatively consistent with the overlimiting differential resistance for three ionic strengths. Hence, the shifting of this overlimiting solution by the critical voltage value yields the complete theoretical description of the entire *I-V* curve. Figure 6(b) further illustrates these transitions for the particular case of 0.07 mM concentration, where the only fitting parameter was the ion mobility  $\mu$  and its associated volume charge density  $\Sigma$  obtained from the low  $c_0$  data of Fig. 5. The limiting-current density of Eq. (9) and Ohmic conductance of Eq. (13) are also depicted in Fig. 6(b) and are shown to be reasonable estimates of the transition current to the limiting resistance region and the Ohmic resistance, respectively.

The differential resistance in the limiting resistance and overlimiting regimes can be estimated by a scaling theory of Ben and Chang [4]. Their Cartesian model does not allow for the radial field-line geometry seen in Fig. 3 from the nanoslot to the electrode in the microreservoir. However, when the polarized layer has invaded sufficiently into the diffusion layer and occupied an area comparable to the cross-section area of the microelectrode, which is assumed to be the case for the limiting resistance and overlimiting regions, the radial geometry with the  $\ln(h/L)$  factor evolves into a linear Cartesian geometry described by Ben and Chang's theory. Integrating the current density predicted by Ben and Chang over an electrode height of  $\sim L$ , as is consistent with the device geometry in Fig. 3, we obtain a relationship between the excess current over the limiting current and the potential drop across the polarized layer  $\tilde{V}-V_0$ .

$$(\tilde{I}-\tilde{I}_L)\lambda = 3\pi w D \varepsilon_0 \varepsilon_f (\tilde{V}-V_0)/(4L). \quad (14a)$$

The nanoslot depth  $h$  does not enter explicitly except in the limiting current  $\tilde{I}_L$  and threshold voltage  $V_0$  at which a transition from Ohmic to limiting resistance region occurs. This threshold voltage due to the development of an extended polarized layer, as the controlling resistance switches from the intraslot region to the polarized layer region, can be estimated from the dimensional versions of the limiting current (9) and the nanoslot conductance (13) as

$$V_0 = -\frac{\pi}{\ln(h/L)} \left( \frac{\eta+1}{\eta-1} \right) (2F\mu\sqrt{(\tilde{\Sigma}/2)^2 + c_0^2 wh/d})^{-1}, \quad (14b)$$

yielding a reasonable agreement to the empirically determined values of Fig. 1(a) (i.e., the first inflection point of the experimental *I-V* curve). Hence, for  $c_0=0.06$  mM—Eq. (14b) yields  $V_0(\text{model})=3.0$  V versus the empirical value of  $V_0(\text{exp})=7.0$  V; for  $c_0=0.07$  mM— $V_0(\text{model})=3.5$  V versus  $V_0(\text{exp})=6.0$  V; and for  $c_0=0.1$  mM— $V_0(\text{model})=5.1$  V versus  $V_0(\text{exp})=8.0$  V. Note, however, that neither empirical values of  $V_0$  or  $\tilde{I}_L$  were used in the computed curves of Fig. 1(a) based on the pseudo-one dimensional model [Eqs. (1)–(5)], which are in a fairly good agreement with the experimental data.

However, the approximation in Eq. (14a) affords an explicit expression for the differential resistances in the limiting resistance and overlimiting regions  $d\tilde{V}/d\tilde{I}=4L\lambda/(3\pi w D \varepsilon_0 \varepsilon_f)$ . Rescaling the experimental *I-V* data of Fig. 1a in Fig. 1(b) using the empirical values of  $\tilde{I}_L$  and  $V_0$  for each ionic strength, successfully collapse both non-Ohmic regimes, the limiting resistance region with  $L=L_{\text{electrode}}=0.8$  mm and the overlimiting region with  $L=L_{\text{instability}}=0.1$  mm, onto the constant differential resistance lines (14a). Using, instead, the theoretical predictions of  $\tilde{I}_L$  Eq. (9) and  $V_0$  Eq. (14b) still collapse the data on the same differential resistance values, as these are independent of  $\tilde{I}_L$  and  $V_0$ . However, in this case, the empirical data are shifted from the predictive differential resistance lines (in both  $x$  and  $y$  coordinates) by the difference between the empirical and theoretical values. Hence, it is clear that both non-Ohmic differential resistance values scale linearly with respect to  $L\lambda$ , as predicted by Ben and Chang [4]. The constant differential resistance line for the overlimiting region in Fig. 1(b) was shifted empirically by a value which approximates the average overvoltage (i.e., the difference between the critical voltage for the emergence of the overlimiting region to that of  $V_0$ —the emergence of the limiting resistance region). That the same scaling but with different  $L$  collapse the data both in the limiting resistance and overlimiting regions for a range of ionic strengths suggests that both involve the same mechanisms for ion currents with the polarized layer being the current controlling region. While the vortices selects the new length scale, its convection does not contribute significantly to the ion current in the microreservoir.

## VI. CONCLUDING REMARKS

Thus, using a nanoslot model and a nonequilibrium ion transport theory, we attribute the nonlinear resistance to an interplay between intraslot ion transport, where at low concentrations the conductivity is dominated by the surface charge and transport across a CPL. The latter extends to the electrodes at the low-voltage window where an Ohmic *I*-*V* regime evolves into one with a large limiting differential resistance, which cannot be captured by the classical limiting-current theories. Beyond a critical voltage, when the vortex instability of a polarized layer sustains a thinner diffusion layer, another regime is approached with a much lower overlimiting resistance comparable to the Ohmic value. Even though we obtained  $L$  for the limiting differential resistance region empirically, we have shown that it can be adequately described by the distance from the membrane-electrolyte interface to the electrode  $L_{\text{electrode}}$ . The only unknown parameter in our numerical pseudo-one-dimensional model that controls the overlimiting region is hence  $L_{\text{instability}}$ , which was determined from the direct experimental measurement [9] [Fig. 2(c)]. A valuable contribution would be to determine  $L_{\text{instability}}$  theoretically to obtain an explicit prediction like that for  $V_0$  in Eq. (14b). A more precise extension of

Ben and Chang's scaling theory [4] to the radial geometry would also be useful. An extension of the current two-dimensional geometry of a wide nanoslot to the three-dimensional geometry of a thin nanoslot (wherein lateral boundaries cannot be neglected) or a nanopore (out of the many existing in a nanoporous membrane) that exists into a microreservoir is most desirable.

Being able to understand the various *I*-*V* regimes of an ion-exchange membrane and nanochannel system is both industrially important and scientifically interesting because of the myriad of pertinent engineering applications due to the very high ion flux that is sustained at the overlimiting region. While the molecular voltage-gating mechanisms of ion channels on cell membranes are probably different from those for the nanoslot, the CPL-dominated interfacial mechanisms with microvortices may also play a role there and could be analyzed in a similar manner.

## ACKNOWLEDGMENT

We are grateful to Professor Y. Zhu and Professor A. Seabaugh of Notre Dame for the use of their equipment and for their advice.

- 
- [1] F. Maletzki, H.-W. Rosler, and E. Staude, *J. Membr. Sci.* **71**, 105 (1992).
  - [2] V. G. Levich, *Physicochemical Hydrodynamics* (Prentice-Hall, New York, 1962).
  - [3] I. Rubinstein and L. Shtilman, *J. Chem. Soc., Faraday Trans. 2* **75**, 231 (1979).
  - [4] Y. Ben and H.-C. Chang, *J. Fluid Mech.* **461**, 229 (2002).
  - [5] J. A. Manzanares, W. D. Murphy, S. Mafe, and H. Reiss, *J. Phys. Chem.* **97**, 8524 (1993).
  - [6] I. Rubinstein, E. Staude, and O. Kedem, *Desalination* **69**, 101 (1988).
  - [7] B. Zaltzman and I. Rubinstein, *J. Fluid Mech.* **579**, 173 (2007).
  - [8] I. Rubinshtein, B. Zaltzman, J. Pretz, and C. Linder, *Russ. J. Electrochem.* **38**, 853 (2002).
  - [9] G. Yossifon and H.-C. Chang, *Phys. Rev. Lett.* **101**, 254501 (2008).
  - [10] D. Stein, M. Kruithof, and C. Dekker, *Phys. Rev. Lett.* **93**, 035901 (2004).
  - [11] Q. Pu, J. Yun, H. Temkin, and S. Liu, *Nano Lett.* **4**, 1099 (2004).
  - [12] A. Plecis, R. B. Schoch, and P. Renaud, *Nano Lett.* **5**, 1147 (2005).
  - [13] R. Karnik, C. Duan, K. Castelino, H. Daiguji, and A. Majumdar, *Nano Lett.* **7**, 547 (2007).
  - [14] S. J. Kim, Y. C. Wang, J. H. Lee, H. Jang, and J. Han, *Phys. Rev. Lett.* **99**, 044501 (2007).
  - [15] V. G. Kutchoukov, F. Laugere, W. van der Vlist, L. Pakula, Y. Garini, and A. Bossche, *Sens. Actuators, A* **114**, 521 (2004).
  - [16] I. Rubinstein and B. Zaltzman, *Phys. Rev. E* **62**, 2238 (2000).
  - [17] S. S. Dukhin, *Adv. Colloid Interface Sci.* **35**, 173 (1991).
  - [18] *CRC Handbook of Chemistry and Physics*, 63th ed., edited by R. C. Weast (CRC, Boca Raton, 1982).
  - [19] R. Karnik, R. Fan, M. Yue, D. Li, P. Yang, and A. Majumdar, *Nano Lett.* **5**, 943 (2005).
  - [20] R. F. Probstein, *Physicochemical Hydrodynamics—An Introduction* (Butterworths, Boston, 1989).